J Electroceram (2010) 24:331–344
DOI 10.1007/s10832-009-9579-6

The development of novel trivalent ion conducting solids and their application for gas sensors

Nobuhito Imanaka · Shinji Tamura

Received: 27 December 2006 / Accepted: 7 May 2009 / Published online: 26 May 2009

Abstract An exceptionally high Al^{3+} ion conducting polycrystalline solid based on the NASICON type structure was successfully realized within the system $(Al_xZr_{1-x})_{4/(4-x)}Nb(PO_4)_3$. The partial substitution of the smaller higher valent Nb^{5+} ion for Zr^{4+} helped stabilize and accommodate the mobile Al^{3+} ion into the NASICON like structure. The addition of boron oxide to the Al^{3+} ion conducting solid electrolyte, as a sintering additive, aided in the achievement of satisfactory mechanical strength and density for practical use. Environmental gas sensors were fabricated by combining the $(Al_xZr_{1-x})_{4/(4-x)}Nb(PO_4)_3$ solid electrolyte with yttria stabilized zirconia (YSZ) and appropriate auxiliary electrodes. The Nernst-like electrochemical sensors demonstrated rapid and reproducible response to CO_2 and NOx, thereby promising excellent potential for environmental monitoring applications.

Keywords Ion conducting solids · Solid electrolytes · Trivalent · Gas sensors · Carbon dioxide · Nitrogen oxides

1 Novel trivalent ion conducting solids

1.1 Introduction

Solid electrolytes are representative of functional materials with important industrial applications including batteries, fuel cells and sensors. A key outstanding characteristic of these materials is that only a single ionic species can rapidly migrate in these solids [1, 2]. However, until recently, highly conducting ions have been largely limited to mono or divalent ionic species. Trivalent rare earth (RE) ions, ion exchanged with Na^+ in some systems, are reported to exhibit reasonably high levels of conductivity. However, a significant Na^+ ion residue remains, contributing to mixed RE^{3+} and Na^+ conduction [3]. As a consequence, purely highly trivalent ion conducting solids have not been realized until recently.

In 1995, a solid exhibiting highly conducting Sc^{3+} ions was demonstrated for $Sc_2(WO_4)_3$ single crystals [4]. This was followed by the identification, by our group, of solids which conduct predominantly by Al^{3+} [5], In^{3+} [6], and other rare earth ion species [7–11]. The tungstate series $(M_2(WO_4)_3)$, has a quasi-two dimensional layered structure, suitable for ion migration in the crystal structure. In addition, hexa-valent tungsten ions strongly bond to oxide ions, as a result, the M^{3+} ions are able to migrate readily in the layered structure. Among trivalent cations, probably the most important industrially is the common metal ion Al^{3+} given its importance in the manufacture of light weight structural elements, beverage containers, oxidation resistant structures, etc. The first trivalent Al^{3+} ion conductor reported by us was in the above introduced $Al_2(WO_4)_3$ system, with an electrical conductivity of 3.2×10^{-6} S·cm^{-1} at 600°C [5]. This remains considerably below $> 10^{-4}$ S·cm^{-1}, a value more in line with values exhibited by commercialized solid electrolytes such as yttria stabilized (YSZ) and calcia stabilized zirconia (CSZ) [12].

For the purpose of realizing a practical Al^{3+} ion conducting solid electrolyte, NASICON (denotes $\underline{Na}^+$ $\underline{S}$uper $\underline{I}$on $\underline{CON}$ductor) [13], composed of a three dimensional network structure that is more suitable as compared with a two-dimensional layered structure, was chosen in our study given its rather open crystallographic structure. This is

N. Imanaka (✉) · S. Tamura
Department of Applied Chemistry, Faculty of Engineering,
Osaka University,
2-1 Yamadaoka, Suita,
Osaka 565-0871, Japan
e-mail: imanaka@chem.eng.osaka-u.ac.jp

particularly true since, in most of cases, specimens are in polycrystalline form with axes randomly ordered leading to significant grain boundary blocking in one or two dimensional structures. The initial focus was on the $M_{1/3}Zr_2(PO_4)_3$ system that offered needed compositional flexibility [14, 15]. During the attempted synthesis, it was found that the Al^{3+} ionic size (ionic radius: 0.0675 nm) [16] was too small to stabilize the $Al_{1/3}Zr_2(PO_4)_3$ based NASICON lattice structure. Therefore, the smaller penta-valent Nb^{5+} cation (ionic radius: 0.078 nm) [16] was partially substituted for Zr^{4+} (ionic radius: 0.086 nm) [16] in order to shrink the NASICON lattice and thereby stabilize the Al containing structure. Penta-valent Nb's higher valence state contributes to improved chemical stability as well as stabilization of the NASICON crystal lattice.

In this article, we discuss the novel $(Al_xZr_{1-x})_{4/(4-x)}Nb(PO_4)_3$ NASICON type system, exhibiting levels of Al^{3+} ion conductivity of practical importance. Specifically we focus on applications of this material for use in environmental gas sensors designed to detect CO_2 and NOx.

1.2 Experimental

The starting materials $Al(OH)_3$, ZrO_2, Nb_2O_5, and $(NH_4)_2HPO_4$ were weighed in a stoichiometric ratio and then mixed in an agate mortar. The pulverized powder was pressed into pellets and heated at 1000°C for 12 h, 1200°C for 12 h, and then 1300°C for 12 h in air. The prepared $(Al_xZr_{1-x})_{4/(4-x)}Nb(PO_4)_3$ samples were pulverized, again pelletized and sintered at 1300°C for 12 h in air. In addition, the $(Al_{0.2}Zr_{0.8})_{20/19}Nb(PO_4)_3$ powder was thoroughly mixed with various amounts of B_2O_3 (99.99 %) and pressed into pellets and sintered at 1300°C for 12 h with an intermediate hold at 850°C for 12 h in air atmosphere.

The X-ray powder diffraction analysis (MultiFlex, using Cu-Kα radiation, Rigaku) was carried out for structural analysis. Electrical conductivity values were derived from measurements performed by applying complex impedance measurements (Hewlett-Packard 4192A) on platinum electroded sintered pellets over the frequency range of 5 Hz to 13 MHz and over the temperature range between 300 and 600°C. Polarization measurements were performed by passing a dc current of 1 μA between two platinum mesh electrodes sandwiching the pellet and monitoring the dc voltage as a function of time in oxygen or helium atmosphere. I–V measurements were also carried out at 800°C in air atmosphere. In order to identify the conducting species in the solids, dc electrolysis was performed by applying a dc voltage of 2.5–3.0 V at 800°C in air across two thick ion-blocking platinum electrodes, while the elemental analysis of the electrolyzed sample was carried out by electron probe microanalysis (EPMA) (EPMA-1500, Shimadzu).

1.3 Results and discussions

Figure 1 shows the trivalent ion conductivity at 600°C as a function of ionic radius for ions in the quasi-two dimensional layered $Sc_2(WO_4)_3$ type and the three dimensional network $M_{1/3}Zr_2(PO_4)_3$ type series [17]. With decreasing ionic radius of the conducting trivalent cations, the ion conductivity increases and shows a peak for Sc^{3+} (ionic radius: 0.0885 nm) [16] in both series. However, the ion conductivity at 600°C is still lower than 10^{-4} S·cm^{-1} and substantially below those of commercially produced stabilized zirconias (shaded area) such as yttria and calcia stabilized zirconia [12]. As discussed above, Al^{3+} is too small in ionic size to form the NASICON type $Al_{1/3}Zr_2(PO_4)_3$ structure without the addition of the smaller pentavalent Nb^{5+} cation.

The relationship between the electrical conductivity and the Al content in the $(Al_xZr_{1-x})_{4/(4-x)}Nb(PO_4)_3$ series is presented in Fig. 2 [17]. The Al^{3+} ion conductivity was highest for $(Al_{0.2}Zr_{0.8})_{20/19}Nb(PO_4)_3$ among the $(Al_xZr_{1-x})_{4/(4-x)}Nb(PO_4)_3$ series having the NASICON type structure. From the X-ray powder diffraction measurements, single phase NASICON type structure was obtained only for $(Al_xZr_{1-x})_{4/(4-x)}Nb(PO_4)_3$ with x=0.1 and 0.2 while samples with x higher than 0.3 consisted of a two phase mixture of the NASICON phase and $NbPO_5$. The secondary $NbPO_5$ phase is insulating and appreciably reduces the ion conductivity.

The relationship between the electrical conductivity and the oxygen partial pressure (PO_2) for $(Al_{0.2}Zr_{0.8})_{20/19}Nb(PO_4)_3$ was investigated at 600°C and the result is presented in Fig. 3. The conductivity reamins nearly constant for the

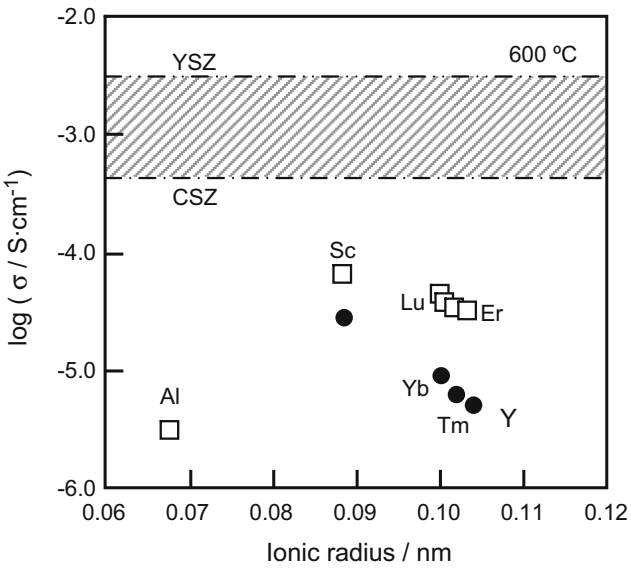

Fig. 1 The trivalent ion conductivity for the $M_2(WO_4)_3$ type (□) and the $M'_{1/3}Zr_2(PO_4)_3$ type series (●) (M=Al, Sc, Lu, Yb, Tm, or Er, M'=Sc, Yb, Tm, or Y) electrolyte at 600°C. (Reproduced with permission from [17]. Copyright 2002 American Chemical Society)

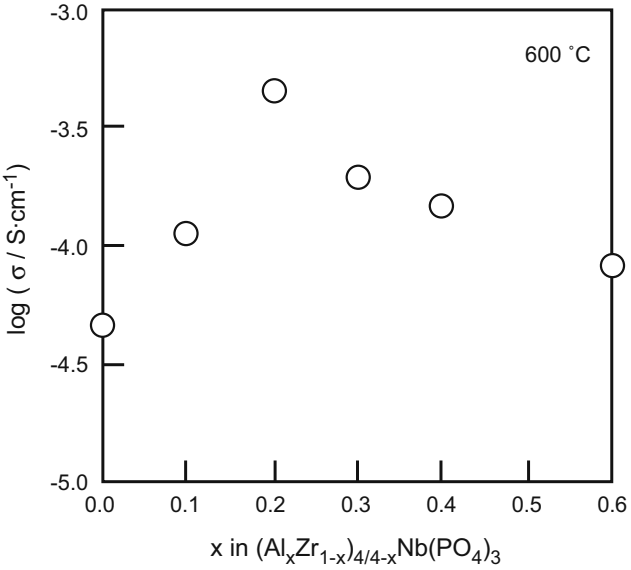

Fig. 2 The Al^{3+} ion conductivity variation with Al concentration for $(Al_xZr_{1-x})_{4/(4-x)}Nb(PO_4)_3$. (Reproduced with permission from [17]. Copyright 2002 American Chemical Society)

whole oxygen pressure region investigated, indicating that the predominant conducting species is ionic in the PO_2 range of between 10^5 and 10^{-16} Pa.

For the purpose of investigating the polarization behavior, the dc to ac conductivity ratio (σ_{dc}/σ_{ac}) was measured as a function of time in both oxygen and helium atmospheres. In the case of electronic conductors, the dc and ac conductivity are equivalent in both atmospheres and the σ_{dc}/σ_{ac} ratio maintains a constant value of unity in any atmosphere since the electron can be supplied in a constant rate. In the case of O^{2-} ion conductors, assuming a reversible electrode, the dc and ac conductivity can be equivalent in an oxygen atmosphere because the migrating O^{2-} ion can be supplied from the ambient oxygen gas. In contrast, in the case of cation conductors (except for protons), the σ_{dc}/σ_{ac} ratio decreases in both atmospheres since cationic species can not be supplied from the ambient atmosphere. In this case, a clear polarization behavior is observed.

The time dependencies of the dc to ac conductivity ratio (σ_{dc}/σ_{ac}) for $(Al_{0.2}Zr_{0.8})_{20/19}Nb(PO_4)_3$ in oxygen and helium atmospheres at 600°C are shown in Fig. 4. The σ_{dc}/σ_{ac} ratio decreases with time in both atmospheres and this result is consistent with the fact that the predominant conducting species in the $(Al_{0.2}Zr_{0.8})_{20/19}Nb(PO_4)_3$ solid is limited to cations. In addition, the cation transference number is estimated to be higher than 0.998, from the σ_{dc}/σ_{ac} ratio after 30 min (ca. 0.002) in both atmospheres.

The temperature dependence of the Al^{3+} ion conductivity in $(Al_{0.2}Zr_{0.8})_{20/19}Nb(PO_4)_3$ is depicted in Fig. 5 with corresponding data for $Al_2(WO_4)_3$ ($Sc_2(WO_4)_3$ structure type) [5]. The Sc^{3+} ion conductivity data for $Sc_2(WO_4)_3$ and $Sc_{1/3}Zr_2(PO_4)_3$, with the optimum ion conductivity among both series (see Fig. 1), are also plotted. The Al^{3+} ion conductivity in this system is more than two orders of magnitude higher than that reported for Al^{3+} in $Al_2(WO_4)_3$ [5] and still more than one order of magnitude higher than that of Sc^{3+} in the $Sc_{1/3}Zr_2(PO_4)_3$ electrolyte which formerly had the optimum trivalent ion conductivity among the NASICON type $M_{1/3}Zr_2(PO_4)_3$ solids. Of particular interest is that the Al^{3+} ion conductivity in $(Al_{0.2}Zr_{0.8})_{20/19}Nb(PO_4)_3$ now even compares favorably with the typical oxide anion conductors YSZ and CSZ [12].

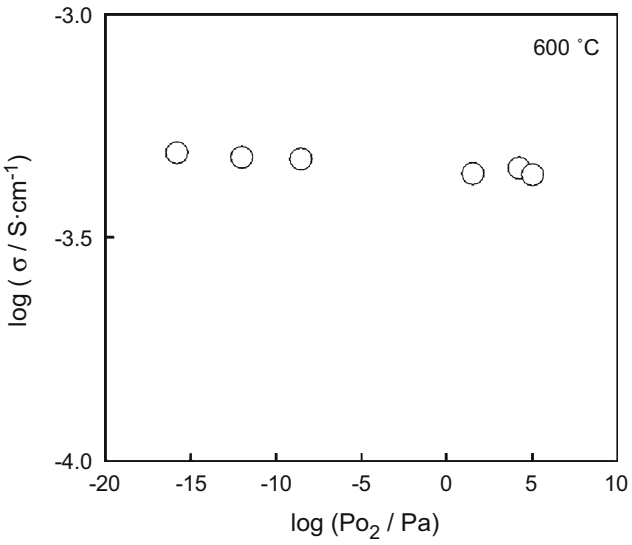

Fig. 3 Oxygen partial pressure dependencies of the ac conductivity for $(Al_{0.2}Zr_{0.8})_{20/19}Nb(PO_4)_3$ at 600°C

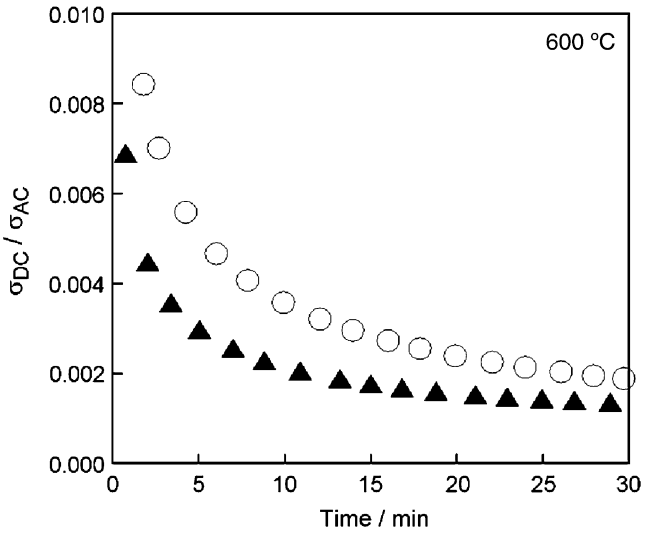

Fig. 4 Time dependencies of the dc to ac conductivity ratio for $(Al_{0.2}Zr_{0.8})_{20/19}Nb(PO_4)_3$ in oxygen (*open circles*) and helium (*closed triangles*) atmospheres at 600°C

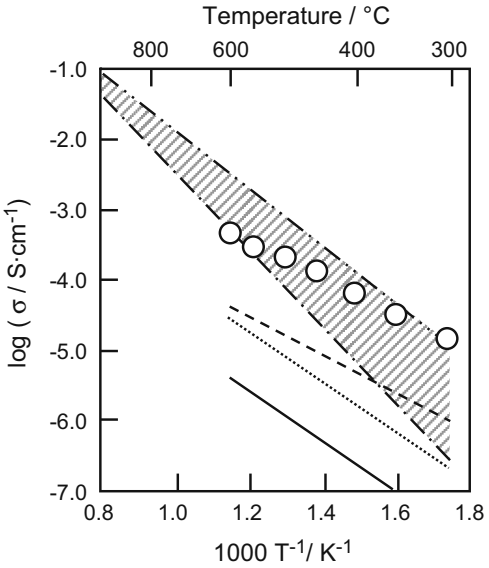

Fig. 5 The temperature dependencies of the Al^{3+} ion conductivity of $(Al_{0.2}Zr_{0.8})_{20/19}Nb(PO_4)_3$ (○) with the data of the Al^{3+} ion conducting $Al_2(WO_4)_3$ solid with the $Sc_2(WO_4)_3$ type structure (—) and the data for $Sc_2(WO_4)_3$ (– –) and $Sc_{1/3}Zr_2(PO_4)_3$ (····) which possess the maximum trivalent ion conductivity among the series. Similar data for YSZ (–··–) and CSZ (–·–) were also drawn. (Reproduced with permission from [17]. Copyright 2002 American Chemical Society)

For the purpose of confirming that Al is the predominant migrating species, dc electrolysis was conducted by applying 3 V, a value above the decomposition potential (ca. 1 V) of $(Al_{0.2}Zr_{0.8})_{20/19}Nb(PO_4)_3$. From the preliminary I–V characteristic measurements, the decomposition voltage of $(Al_{0.2}Zr_{0.8})_{20/19}Nb(PO_4)_3$ was obtained (see Fig. 6). The current increases by applying more steeply as the voltage exceeds 1.4 V. Thus, the decomposition voltage of $(Al_{0.2}Zr_{0.8})_{20/19}Nb(PO_4)_3$ was determined to be approximately 1.4 V. Following electrolysis, precipitates were clearly observed on the cathodic surface. EPMA spot analysis of the deposits confirmed high Al segregation as listed in Table 1 [17] with the Al content more than 20 times higher compared to the Al content before electrolysis. In contrast, the ratio of other cation elements of Zr, Nb, and P measured after and before electrolysis appreciably decreased. The results of the EPMA line measurements of the electrolyzed pellet are depicted in Fig. 7 [17]. High Al segregation was observed near the cathodic surface (shaded area), but not for Zr, Nb, or P. From the polarization analysis (see Fig. 4), the ion transference number estimated is higher than 0.998 and one can conclude that the predominant migrating species in $(Al_{0.2}Zr_{0.8})_{20/19}Nb(PO_4)_3$ is the trivalent Al^{3+} ion.

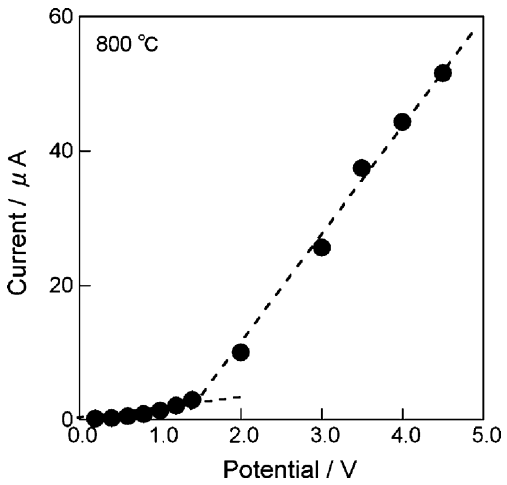

Fig. 6 I–V relationship for $(Al_{0.2}Zr_{0.8})_{20/19}Nb(PO_4)_3$ at 800°C

While the magnitude of the Al^{3+} conductivity of $(Al_{0.2}Zr_{0.8})_{20/19}Nb(PO_4)_3$ now appears to be adequate for practical applications, improvements in mechanical strength and density are desired, especially for use as a miniaturized sensor element. Towards this end, the sintering additive B_2O_3 was investigated to achieve improved microstructures [18]. The advantage of the B_2O_3 addition is reported in detail in [19].

Figure 8 presents the temperature dependencies of the Al^{3+} ion conductivity for both $(Al_{0.2}Zr_{0.8})_{20/19}Nb(PO_4)_3$, with and without the addition of 6 wt% B_2O_3 [19]. The conductivity of the $(Al_{0.2}Zr_{0.8})_{20/19}Nb(PO_4)_3$ sample with B_2O_3 is approximately twice as high as that of the sample without B_2O_3 at 600°C. This conductivity enhancement is mainly ascribed to the improvement of sinterability by decreasing the pore volume in the sintered pellet and also enhancing the contact between grains.

2 Gas sensor application

2.1 CO_2 gas sensor

2.1.1 Introduction

CO_2 gas emission causes a serious environmental problem, the "Greenhouse effect", and therefore, the suppression of

Table 1 The results of EPMA spot analyses on the cathodic surface deposits after electrolysis.

Element	Atomic percent		
	Before	After	
		Cathode (Area 1)	Cathode (Area 2)
Al	4.1	88.8	82.6
Zr	16.7	0.2	0.2
Nb	19.8	6.1	7.8
P	59.4	4.9	9.4

(Reprinted with permission from [17]. Copyright 2002 American Chemical Society.)

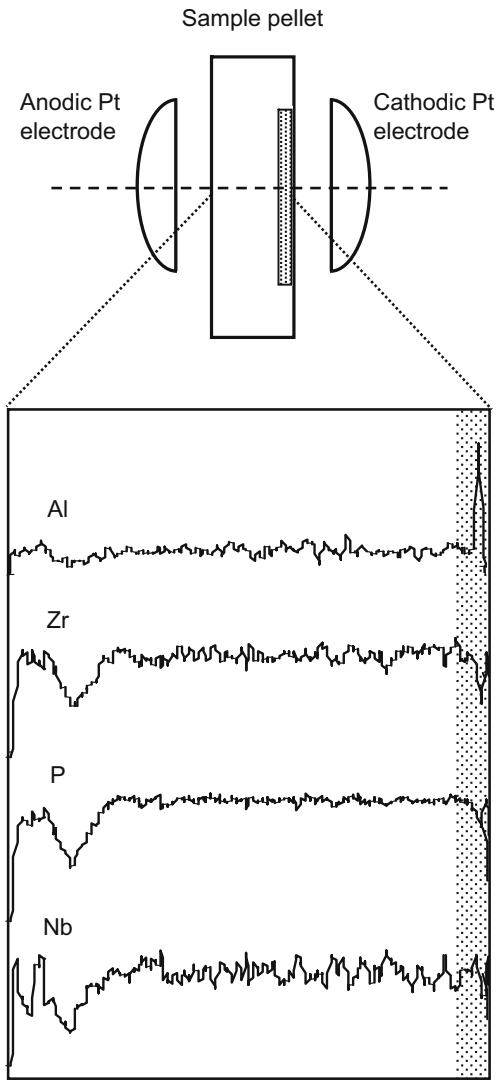

Fig. 7 The results of the line EPMA measurements for the electrolyzed $(Al_{0.2}Zr_{0.8})_{20/19}Nb(PO_4)_3$ sample. (Reproduced with permission from [17]. Copyright 2002 American Chemical Society)

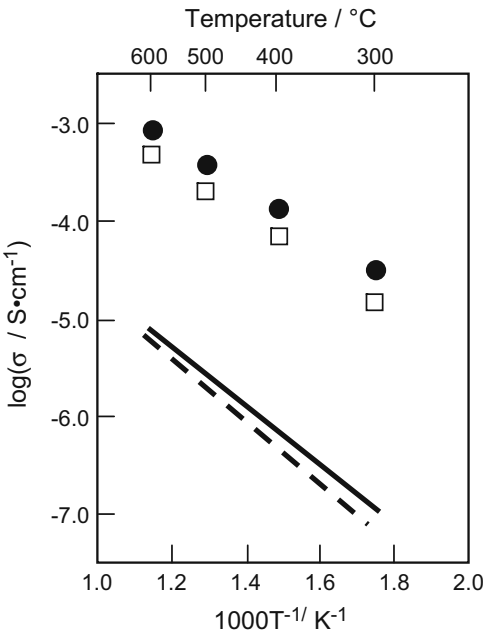

Fig. 8 Temperature dependencies of the ion conductivity for $(Al_{0.2}Zr_{0.8})_{20/19}Nb(PO_4)_3$ with the addition of 6 wt% B_2O_3 (●) and the sample without B_2O_3 addition (□) previously reported [18], with the conductivity data for ZrP_2O_7 (—), and $P_2O_5{\cdot}9Nb_2O_5$ (— —). (Reproduced with permission from [19])

CO_2 exhaust is an urgent issue. An effective approach to suppress CO_2 gas emission into the atmosphere is on-site monitoring and control of the combustion conditions. Although IR absorption has been successfully applied for CO_2 gas detection, such optical devices are too expensive to install at every CO_2 gas emitting site. As a lower cost alternative, electrochemical CO_2 gas sensors based on monovalent [20–24] and divalent [25–27] cation conducting oxides have been proposed. However, these materials suffer from insufficient long term stability and/or selectivity. For example, the sensing auxiliary electrodes needed for their operation are typically alkaline metal carbonates which easily react with other gases such as ambient water vapor and, as a result, causes serious deterioration of sensing performance. Recently, we proposed a more robust CO_2 gas sensor using a trivalent ion conducting solid electrolyte and yttria stabilized zirconia (YSZ) together with the $(Nd_{0.47}Ba_{0.12}Li_{0.29})_2O_{0.94}CO_3$ sensing auxiliary electrode, an insoluble compound. [28, 29]. By applying the trivalent Al^{3+} ion conducting solid electrolyte and yttria stabilized zirconia, the compound formed between them is aluminum oxide (Al_2O_3). On the other hand, in the case that a monovalent Na^+ ion conducting solid electrolyte such as NASICON is utilized, the compound formed is sodium oxide (Na_2O) which easily reacts with carbon dioxide and water vapor to form carbonates and hydroxides. This is described in the following, beginning with a discussion related to the selection and optimization of the stable auxiliary electrode.

A key factor limiting realization of a practical CO_2 electrochemical-based sensor is the instability of the auxiliary electrode with respect to water vapor. Table 2 tabulates the solubility of carbonate based compounds in

Table 2 Solubility in 100 g H_2O at 25°C.

Compounds	Solubility
Li_2CO_3	1.5
$Nd_2O_2CO_3$	3.2×10^{-4}
$Nd_{2/3}Li_{1/3})_2O_{4/3}CO_3$	6.0×10^{-3}
$(Nd_{0.47}Ba_{0.12}Li_{0.29})_2O_{0.94}CO_3$	1.1×10^{-4}

(Reprinted with permission from [27]. Copyright 2002 American Chemical Society.)

100 g water [27]. Even though lithium carbonate is the least soluble in water amongst the alkaline metal carbonates, it still remains relatively high at 1 g. On the other hand, the neodymium oxycarbonate $Nd_2O_2CO_3$, has a much lower solubility of 3.2×10^{-4} g. To obtain a Li containing auxiliary electrode with reduced water solubility, Li_2CO_3 was mixed with $Nd_2O_2CO_3$ to form the solid solution $(Nd_{2/3}Li_{1/3})_2O_{4/3}CO_3$ which resulted in an intermediate solubility of 10^{-3} g. To further reduce the solubility in water, $BaCO_3$, which is extremely insoluble in water, was mixed with $(Nd_{2/3}Li_{1/3})_2O_{4/3}CO_3$ to form the $(Nd_{0.47}Ba_{0.12}Li_{0.29})_2O_{0.94}CO_3$ solid solution with the low solubility of 1.1×10^{-4} g.

While the CO_2 gas sensor with the $(Nd_{0.47}Ba_{0.12}Li_{0.29})_2O_{0.94}CO_3$ auxiliary sensing electrode was found to exhibit superior sensing performance including high selectivity and reproducible response, the sensor would only operate properly at elevated temperature in the vicinity of 550°C. Lower temperature operation is, however, desirable to insure the stabilization of the sensor element interfaces between the electrolytes, and between the electrolyte and electrode and long term operating stability. Lower temperature operation is expected to be improved by increasing the conductivity of the sensing auxiliary electrode.

2.1.2 Experimental

Lanthanum oxysulfate was obtained by heating La_2S_3 at 1000°C for 12 h in air. The prepared $La_2O_2SO_4$ sample was mixed with Li_2CO_3 in a molar ratio of 8:2 and heated at 650°C for 12 h in a nitrogen atmosphere. The $0.8La_2O_2SO_4$–$0.2Li_2CO_3$ sample was mixed with $(Nd_{0.47}Ba_{0.12}Li_{0.29})_2O_{0.94}CO_3$ [28, 29] (in a molar ratio of 1:1) and heated at 600°C for 12 h in a nitrogen atmosphere. The $(Al_{0.2}Zr_{0.8})_{20/19}Nb(PO_4)_3$ [17] was prepared as described above. Yttria stabilized zirconia (YSZ) was synthesized by mixing ZrO_2 and Y_2O_3 in a molar ratio of 9:1, and heated at 1600°C for 12 h in air.

Figure 9 presents the cross-sectional view of the CO_2 sensor element [30]. After sintering both $(Al_{0.2}Zr_{0.8})_{20/19}Nb(PO_4)_3$ (1300°C for 12 h) and YSZ (1600°C for 12 h) pellets, the two pellets were tightly fixed by an inorganic adhesive agent. The $0.8La_2O_2SO_4$–$0.2Li_2CO_3$ electrode with $(Nd_{0.47}Ba_{0.12}Li_{0.29})_2O_{0.94}CO_3$ was applied to the Al^{3+} ion conducting solid electrolyte surface as the sensing auxiliary electrode. Platinum and gold guaze were applied as the reference and the detecting electrode, respectively, to realize a suitable contact between the ambient gas species and the electrode. The test gas was regulated by mixing air and 1% CO_2 gas diluted with N_2 and the characteristics of the sensor were examined at 500°C in the CO_2 concentration range from 500 to 3,000 ppm and a total gas flow rate of 200 ml/min. The influence of water vapor on the CO_2 sensing properties was investigated by flowing the mixture

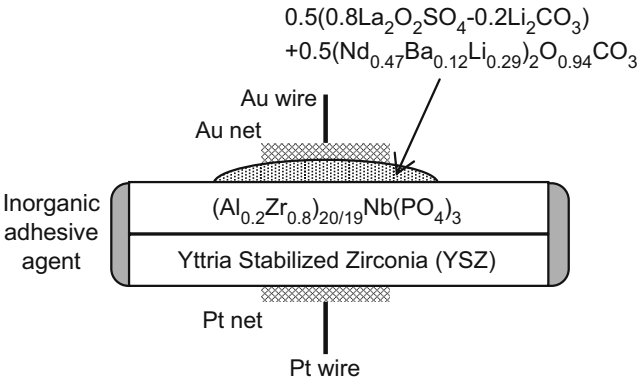

Fig. 9 The cross-sectional view of the CO_2 sensor cell. (Reproduced with permission from [30]. Copyright 2005 Elsevier B. V.)

gas of dry 1% CO_2 gas diluted with N_2 and wet air. Humidified air was obtained by bubbling dry air into water vessel heated to 90°C and then passing it through a water bath at 30°C. The influence of nitrogen monoxide (NO) or oxygen (O_2) gas on CO_2 sensing was also examined by holding the CO_2 gas concentration at 1,000 ppm and changing the NO or O_2 gas concentration from 0 to 600 ppm for NO or between 0 and 40% for O_2, respectively.

The assembly of the sensor cell was carried out as follows. 8 mol% YSZ powder was heated at 1250°C for 2 h. A two layered pellet, ca. 0.4 mm thick, was formed from $(Al_{0.2}Zr_{0.8})_{20/19}Nb(PO_4)_3$ and 8 mol% YSZ powders, both admixed with B_2O_3, by co-pressing into a pellet at 100 kN for 3 min. The cationic/anionic conductor pellet was sintered at 1300°C for 12 h in air atmosphere, and then laser cut (YAG laser) into a segment of 0.5 mm^2. Lanthanum oxysulfate was obtained by heating La_2S_3 powder at 1000°C for 12 h in air and then $La_2O_2SO_4$ was mixed with Li_2CO_3 in a molar ratio of 8:2 and heated at 1000°C for 12 h in air. Here, oxysulfate is utilized instead of the oxycarbonate to achieve higher temperature durability. The platinum thin film heater and gold electrodes were prepared by RF sputtering and dimensioned photolithographically, on an Al_2O_3 substrate (3 mm×2 mm).

The cationic/anionic solid electrolyte segment was attached to the Al_2O_3 substrate with a binder. Li_2CO_3-$La_2O_2SO_4$ and Pt pastes were used as the detecting and reference electrodes, respectively, on either side of the segment and heated at 600°C for an half hour by the heater on the sensor substrate by controlling the input voltage. The operating temperature of the sensor was fixed at 500°C with an electric power consumption of 0.6 W. The CO_2 sensor EMF output was monitored in the CO_2 concentration range from 500 ppm to 3%.

2.1.3 Results and discussions

The bilayer Al^{3+} ion conducting $(Al_{0.2}Zr_{0.8})_{20/19}Nb(PO_4)_3$ and oxide (O^{2-}) ion conducting yttria stabilized zirconia

(YSZ) electrolyte is combined with the CO_2 gas sensing auxiliary electrode $0.5(0.8La_2O_2SO_4\text{-}0.2Li_2CO_3)+0.5(Nd_{0.47}Ba_{0.12}Li_{0.29})_2O_{0.94}CO_3$ (See Fig. 9 [30]). The combination of both $La_2O_2SO_4\text{-}0.2Li_2CO_3$ and $(Nd_{0.47}Ba_{0.12}Li_{0.29})_2O_{0.94}CO_3$ solid solution is applied in order to realize a high chemical reactivity with CO_2 gas at the sensing electrode as well as a high conductivity.

The sensing mechanism of the CO_2 sensor is described in the following. The electrochemical cell is described by:

$$CO_2-\text{air, auxiliary sensing electrode, } Pt\left|(Al_{0.2}Zr_{0.8})_{20/19}Nb(PO_4)_3\right|YSZ|Pt, CO_2-\text{air} \quad (1)$$

(At the auxiliary sensing electrode)

$$Li_2CO_3(\text{in } 0.5(0.8La_2O_2SO_4-0.2Li_2CO_3)+0.5(Nd_{0.47}Ba_{0.12}Li_{0.29})_2O_{0.94}CO_3 \text{ solid}) \leftrightarrow 2Li^+ + CO_2 + 1/2O_2^I + 2e^- \quad (2)$$

(Interface between the auxiliary electrode and Al^{3+} ion conducting solid)

$$2Li^+ + 19/6(Al_{0.2}Zr_{0.8})_{20/19}Nb(PO_4)_3 \leftrightarrow 2/3Al^{3+} + 19/6(Li_{0.6}Zr_{0.8})_{20/19}Nb(PO_4)_3 \quad (3)$$

(Interface between the two electrolytes)

$$2/3Al^{3+} + O^{2-} \leftrightarrow 1/3Al_2O_3 \quad (4)$$

(At the reference electrode)

$$1/2O_2^{II} + 2e^- \leftrightarrow O^{2-} \quad (5)$$

Therefore, the overall reaction is expressed as follows.

$$Li_2CO_3 + 19/6(Al_{0.2}Zr_{0.8})_{20/19}Nb(PO_4)_3 + 1/2O_2^{II} \leftrightarrow CO_2 + 1/2O_2^I + 19/6(Li_{0.6}Zr_{0.8})_{20/19}Nb(PO_4)_3 + 1/3Al_2O_3 \quad (6)$$

From Eq. (6), the following Nernst Eq. (7) is obtained.

$$E = E_0 - (RT/nF)\ln\left\{(P_{CO_2})\cdot\left(P_{O_2^I}\right)^{1/2}\cdot\left(a_{(Li_{0.6}Zr_{0.8})_{20/19}Nb(PO_4)_3}\right)^{19/6}\cdot(a_{Al_2O_3})^{1/3}\cdot(a_{Li_2CO_3})^{-1}\cdot\left(a_{(Al_{0.2}Zr_{0.8})_{20/19}Nb(PO_4)_3}\right)^{-19/6}\cdot\left(P_{O_2^{II}}\right)^{-1/2}\right\}, n = 2.00 \quad (7)$$

Since Li_2CO_3, $(Al_{0.2}Zr_{0.8})_{20/19}Nb(PO_4)_3$, $(Li_{0.6}Zr_{0.8})_{20/19}Nb(PO_4)_3$, and Al_2O_3 are all in a solid state, their chemical activities (a in the Eq. (7)) are constant values at a given temperature. Therefore, the natural logarithm terms of these activities are fixed at constant values. In addition, O_2^I is exactly equivalent to O_2^{II}, because the whole sensor element is exposed to the same ambient atmosphere as shown in Fig. 9. Then, Eq. (7) can be finally simplified as follows.

$$E = E_0' - (RT/nF)\ln(P_{CO_2}), \quad n = 2.00 \quad (8)$$

Figure 10 depicts a typical sensor response curve at 500°C for dry CO_2 gas with concentration between 500 and 3,000 ppm [30]. The response time, defined as the time to attain a 90% EMF response was around 4–5 min, with the sensor showing reproducible and stable sensor EMF output. By miniaturizing the sensor element, the response time reduces to less than 5 s as introduced in Fig. 16 below. The sensor EMF output variations with CO_2 content at 500°C in dry and wet atmospheres are presented in Fig. 11 with the slope (solid line) calculated from Eq. (8) [30]. The EMF values in both atmospheres are nearly identical with a linear relationship between EMF and $\log(Pco_2)$. The number of electrons (n), estimated from the observed slope, was 2.13 and 2.06 for dry and wet atmosphere, respectively. Since these n values are very close to the theoretical value of 2.00, as predicted by the Nernst Eq. (8), this demonstrates that the present sensor can quantitatively detect the CO_2 content without interference from water vapor.

Carbon dioxide gas is emitted by combustion of hydrocarbons. However, because the exhaust gas also contains NO gas and a variable oxygen gas concentration, the stability of the sensor response against NO and O_2 variations is critical

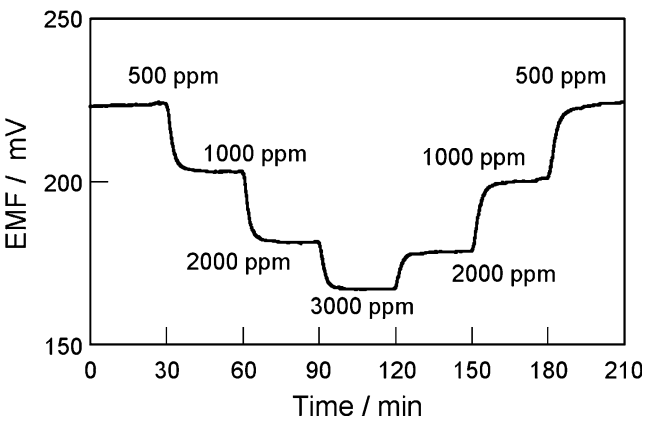

Fig. 10 One of the representative sensor response curves for dry CO_2 gas concentration between 500 and 3,000 ppm at 500°C. (Reproduced with permission from [30]. Copyright 2005 Elsevier B. V.)

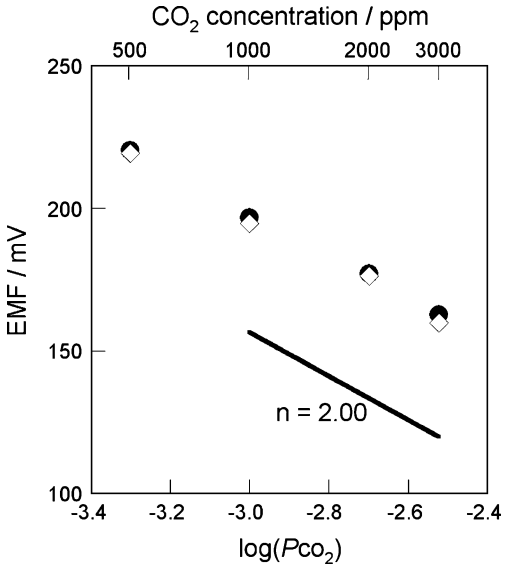

Fig. 11 The sensor output (EMF) variation with the CO_2 concentration at 500°C in dry (●) and wet (◊) atmospheres. (Reproduced with permission from [30] Copyright 2005 Elsevier B. V.)

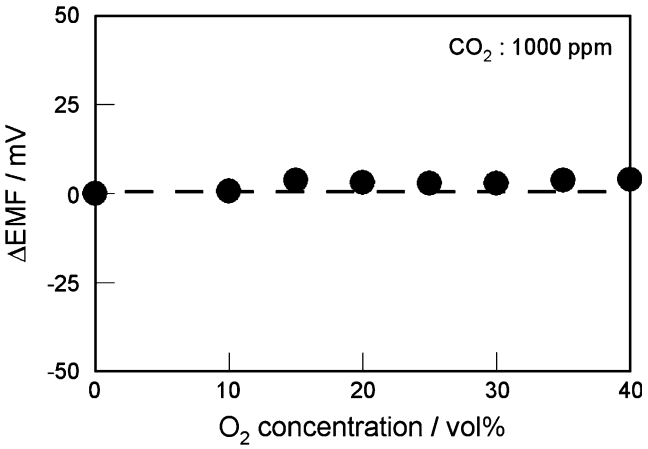

Fig. 13 The sensor output deviation (500°C) with the oxygen content in the atmosphere where CO_2 concentration is constant at 1,000 ppm. (Reproduced with permission from [30]. Copyright 2005 Elsevier B. V.)

for practical sensor application, in addition to insensitivity to water vapor. The EMF output variations with NO and O_2 concentrations in an atmosphere of fixed CO_2 concentration (1,000 ppm) at 500°C are presented in Figs. 12 [30] and 13 [30], respectively. The deviation of sensor output (ΔEMF) from the EMF value obtained in 1,000 ppm CO_2 diluted with dry air is within 1.0 mV for NO and 3.0 mV for O_2, respectively. These deviations of only 0.3% and 0.7% demonstrate that neither NO nor O_2 interfere with the CO_2 sensing performance even in harsh environments where potentially interfering gas concentrations change drastically.

For the purpose of realizing a miniaturized CO_2 sensor chip, the sensor element was down sized as shown schematically in Fig. 14(a) [31], while a photograph of

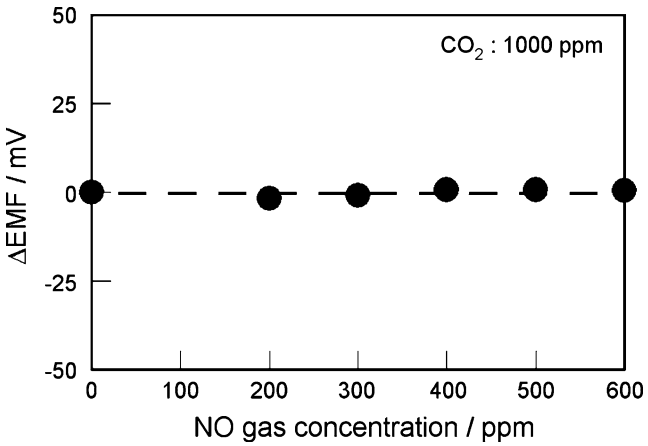

Fig. 12 The sensor output deviation (500°C) with the NO gas concentration in the atmosphere where CO_2 concentration is constant at 1,000 ppm. (Reproduced with permission from [30]. Copyright 2005 Elsevier B. V.)

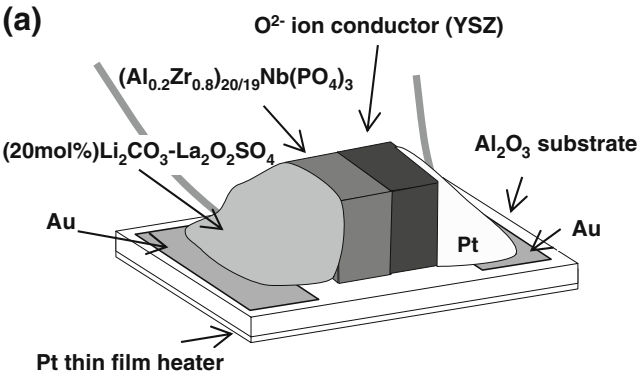

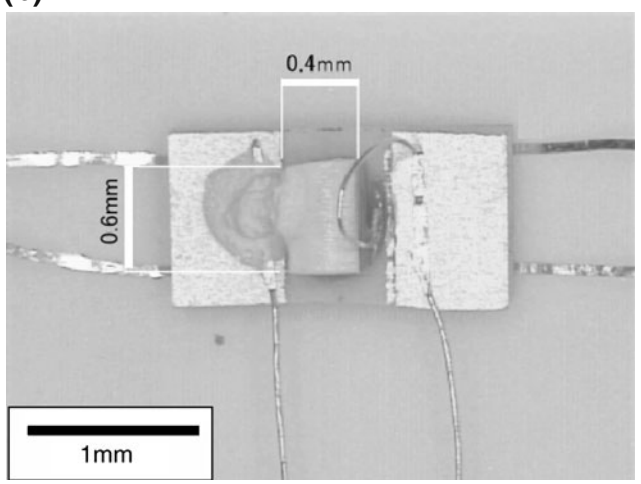

Fig. 14 A schematic illustration of the miniaturized CO_2 sensor cell with thin Pt film heater (**a**) ((Reproduced with permission from [31]. Copyright 2006 The Electrochemical Society of Japan)) and the photograph of the representative miniaturized CO_2 sensor tip (**b**)

the representative miniaturized CO_2 sensor chip is shown in Fig. 14(b) (The $La_2O_2SO_4$-Li_2CO_3 electrode was applied due to the thermal stability reason.). By reducing the sensor dimensions to 2 mm×3 mm×1 mm, the power consumption could be lowered to 0.6 W.

A plausible detection mechanism at the auxiliary electrode is as follows.

(Sensing auxiliary electrode)

$$Li_2CO_3(\text{in } La_2O_2SO_4) \leftrightarrow 2Li^+ + CO_2 + 1/2O_2(I) + 2e^- \quad (9)$$

In fact, the sensor shows excellent gas selectivity to CO_2, and the sensor output follows the following theoretical Nernst equation exceptionally well.

$$E = E_0(\text{constant}) - (RT/nF)\ln(P_{CO_2})(n = 2.00) \quad (10)$$

Figure 15 shows the relationship between the sensor EMF output and the logarithm of the CO_2 content at 500°C [31]. The sensor output decreases with increasing CO_2 gas content with a linear relationship observed between the sensor output and the logarithm of the CO_2 gas concentration. The solid line indicates the slope of the theoretical Nernst relationship as shown in Eq. (10), when the number of electrons transferred is 2.00. The experimentally derived value of 2.02 for the miniaturized sensor element is in very good agreement with the theoretical value.

A typical response sensor curve is presented in Fig. 16 for CO_2 gas concentrations from 500 ppm up to 1% [31]. The sensor demonstrates fast response to CO_2 gas variations with the time to attain 90% of the total response being less than 5 s, as desired for practical devices.

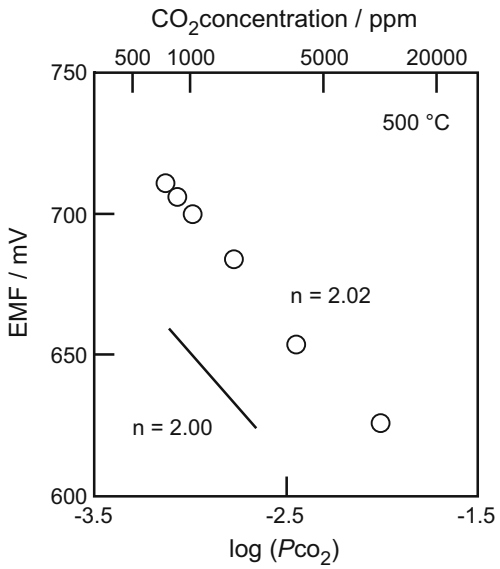

Fig. 15 The relationship between the sensor EMF output and the logarithm of the CO_2 content at 500°C. (Reproduced with permission from [31]. Copyright 2006 The Electrochemical Society of Japan)

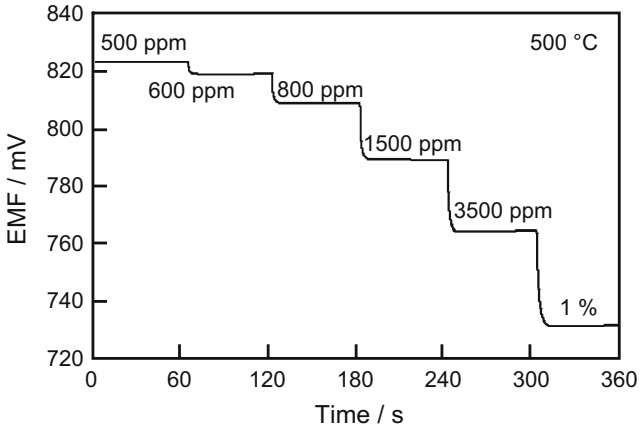

Fig. 16 A typical sensor response curve for CO_2 gas content from 500 ppm to 1%. (Reproduced with permission from [31]. Copyright 2006 The Electrochemical Society of Japan)

Figure 17 shows the long term response of the miniaturized sensor output at the CO_2 concentrations of 500 ppm and 3%, respectively [31]. While the sensor output decreased during the initial 5 days, it subsequently showed stable output for the subsequent 95 days. The annealing-in process is believed necessary for realizing a stable contact between the electrolytes, and between the electrolyte and electrode.

2.2 NOx sensors

2.2.1 Introduction

NO and NO_2 (i.e. NOx) are a major source of air pollution and their suppression has become an urgent health and environmental issue. For this purpose, accurate on-site detection is required. Various types of NOx gas sensors have been proposed. Given promising results, sensors based

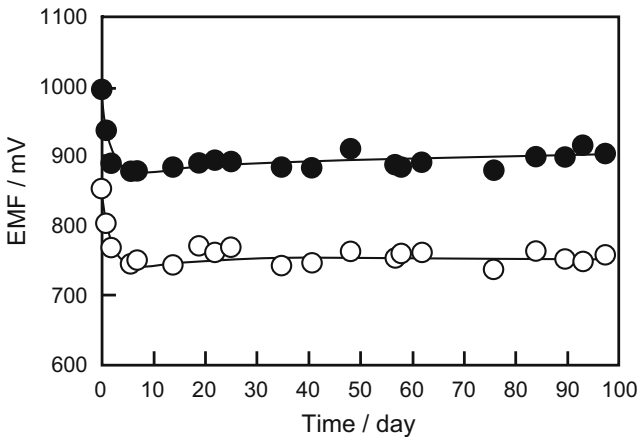

Fig. 17 The long term stability of the sensor EMF output for CO_2 gas content of 500 ppm (●) and 3% (○) . (Reproduced with permission from [31]. Copyright 2006 The Electrochemical Society of Japan)

on solid electrolytes and electrochemical principles have received broad interest [32–41]. Here we report success with the development of a gas sensor suitable for total nitrogen oxide gas sensing (i.e. NO plus NO_2) based on the use of a rare earth based auxiliary electrode in combination with Al^{3+} cation and O^{2-} anion conducting solid electrolytes.

2.2.2 Experiments

The Al^{3+} ion conducting electrolyte and the yttria stabilized zirconia (YSZ) solid electrolyte were prepared as pellets as described above. Gadolinium oxide and potassium nitrite were mixed in a molar ratio of 2:1 and the mixture was ball milled for 12 h in air. The Gd_2O_3 and KNO_2 mixed powder was made into pellets and heated at 450°C for 12 h. During the heat treatment, the KNO_2 oxidizes to KNO_3 and forms a Gd_2O_3-KNO_3 solid solution as confirmed by X-ray powder diffraction.

The two solid electrolyte pellets were attached together by an inorganic adhesive agent and the Gd_2O_3-KNO_3 solid solution electrode was set on the Al^{3+} ion conducting solid surface (see Fig. 18 [42]) and heated up to the operating temperature of 450°C. NO and NO_2 gas concentrations from 200 to 2,000 ppm were regulated by mixing 1% NO or 1% NO_2 diluted with N_2 gas with air, respectively. The total gas flow rate was maintained at 100 ml/min and the sensor EMF output was monitored by an electrometer (Advantest, R8240).

2.2.3 Results and discussions

Table 3 lists the melting point of various candidate alkaline metal nitrites and nitrates to be used in the auxiliary electrode suitable for NOx sensing [42] with potassium nitrite obviously the most thermally durable. This compound was thus used to improve the refractory nature of the

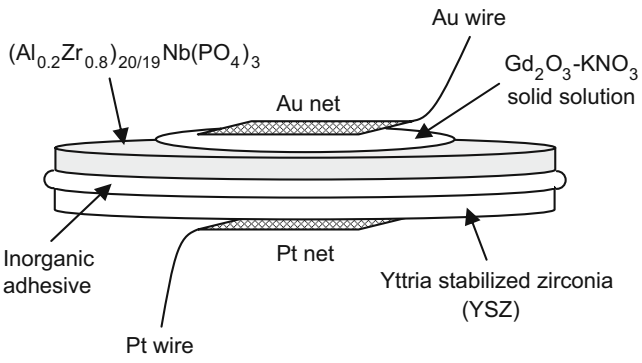

Fig. 18 The overview of the total nitrogen oxide gas sensor with the combination of trivalent Al^{3+} ion conducting solid and O^{2-} ion conducting stabilized zirconia (YSZ) with the Gd_2O_3-KNO_3 solid solution as the auxiliary electrode. (Reproduced with permission from [42]. Copyright 2004 The Electrochemical Society Inc.)

Table 3 Melting point of alkaline metal nitrites and nitrates.

Compounds	Melting point / °C
$LiNO_3$	264
$NaNO_2$	271
$NaNO_3$	306
KNO_2	440
KNO_3	339
$RbNO_3$	330
$CsNO_3$	414

(Reproduced with permission from [42]. Copyright 2004 The Electrochemical Society Inc.)

auxiliary rare earth oxide electrode. Among the three structures that the rare earth oxides crystallize in, i.e., the A, B, and C-types [43], the C-type (cubic) is the lowest in density and has the largest open space in the crystal lattice. Therefore, the C-type structure is expected to be the most suitable candidate for forming the interstitially inserted solid solution of rare earth oxide with potassium nitrate. Among the various solid solutions, the Gd_2O_3-KNO_3 system exhibits the highest K^+ ion conductivity, comparable to that of K^+-β"-alumina single crystal [44], reported to be one of the best K^+ ion conducting solid electrolytes.

From the X-ray powder diffraction results, one observes that the *a* lattice parameter of Gd_2O_3-KNO_3 increases with increasing KNO_3, indicating that the solid solution is successfully obtained. The detailed electrical and structural properties of the Gd_2O_3-KNO_3 system are reported in [45, 46], respectively.

Figure 19 shows a representative sensor response curve to NO concentrations ranging from 200 to 2,000 ppm,

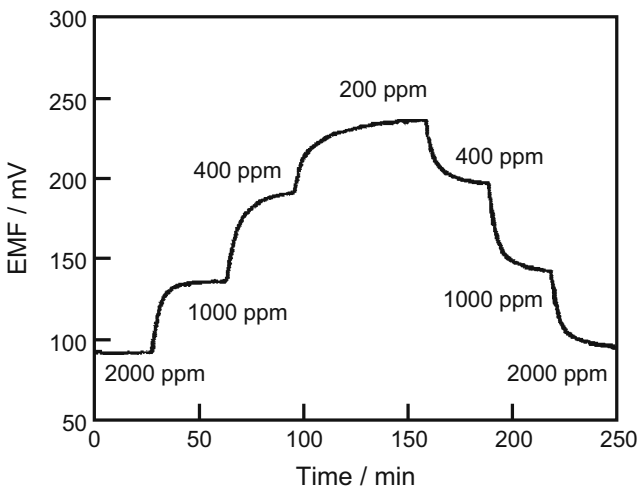

Fig. 19 One of typical sensor output changes with the NO concentration variation (200–2,000 ppm) at 450°C. (Reproduced with permission from [42]. Copyright 2004 The Electrochemical Society Inc.)

typical of concentrations emitted into the atmosphere [42]. The response is observed to be reversible and reproducible. The response time, defined as the time to reach 90% total response, was under 10 min.

The plausible reactions occurring at the detecting Gd_2O_3-KNO_3 auxiliary electrode, the interface between the detecting electrode and the Al^{3+} ion conducting solid electrolyte, the interface between the two solid electrolytes, and the reference electrode include:

(Detecting electrode)

$$KNO_3(\text{in } Gd_2O_3) \leftrightarrow K^+ + NO + O_2^{I} + e^- \quad (11)$$

(Interface between the detecting electrode and the $(Al_{0.2}Zr_{0.8})_{20/19}Nb(PO_4)_3$ electrolyte)

$$K^+ + 19/12(Al_{0.2}Zr_{0.8})_{20/19}Nb(PO_4)_3 \leftrightarrow 1/3Al^{3+} + 19/12(K_{0.6}Zr_{0.8})_{20/19}Nb(PO_4)_3 \quad (12)$$

(Interface between the two solid electrolytes)

$$1/3Al^{3+} + 1/2O^{2-} \leftrightarrow 1/6Al_2O_3 \quad (13)$$

(Reference electrode)

$$1/4O_2^{II} + e^- \leftrightarrow 1/2O^{2-} \quad (14)$$

(O_2^{I} and O_2^{II} denote the oxygen gas appearing on the surface of the detecting auxiliary electrode and the reference electrode, respectively.) Based on Eqs. (11) to (14), the total chemical reaction is summarized as follows.

$$KNO_3 + 19/12(Al_{0.2}Zr_{0.8})_{20/19}Nb(PO_4)_3 + 1/4O_2^{II} \leftrightarrow 1/6Al_2O_3 + 19/12(K_{0.6}Zr_{0.8})_{20/19}Nb(PO_4)_3 + NO + O_2^{I} \quad (15)$$

Then, the following Nernst equation can be derived.

$$E = E_0 - (RT/nF)\ln\left\{(a_{Al_2O_3})^{1/6}\cdot\left(a_{(K_{0.6}Zr_{0.8})_{20/19}Nb(PO_4)_3}\right)^{19/12}\cdot(P_{NO})\cdot\left(P_{O_2^{I}}\right)\cdot(a_{KNO_3})^{-1}\cdot\left(a_{(Al_{0.2}Zr_{0.8})_{20/19}Nb(PO_4)_3}\right)^{-19/12}\cdot\left(P_{O_2^{II}}\right)^{-1/4}\right\} \quad (E_0 = \text{constant}, n = 1.00) \quad (16)$$

The activity of solids is constant if the operating temperature is fixed and both $P_{O2}{}^{I}$ and $P_{O2}{}^{II}$ are equal to 2.1×10^4 Pa since the experiment was carried out in air atmosphere, the above Nernst Eq. (16) can be simplified as the following relation.

$$E = E_0' - (RT/nF)\ln(P_{NO}) \quad \left(E_0' = \text{constant}, n = 1.00\right) \quad (17)$$

The sensor output, depicted in Fig. 19 for increasing and decreasing NO gas concentration, is plotted in Fig. 20 as closed squares and open circles, respectively [42]. The sensor output monotonously reduced with the increase of the NO gas concentration and a linear relation clearly appears in the relationship between the sensor output and the logarithm of the partial pressure of NO (P_{NO}). The slope (with n=1.00) predicted from Eq. (17) is also plotted as a solid line in Fig. 20. The n values obtained from obtaining a best fit of the data for increasing and decreasing P_{NO} , are 1.03 and 1.01, respectively which coincide well with the predicted value of n=1.00 expected from the theoretical Nernst response.

In order to examine the suitability of this sensor for NO_2 gas detection, the sensor was also tested in various NO_2 gas concentrations. A typical response is plotted in the insert of Fig. 21 while the sensor EMF output vs. the logarithm of P_{NO2} is shown in the main part of Fig. 21 [42]. In this case, the plausible reaction postulated in Eq. (11) can be re-written as

$$KNO_3(\text{in } Gd_2O_3) \leftrightarrow K^+ + NO_2 + 1/2O_2 + e^- \quad (18)$$

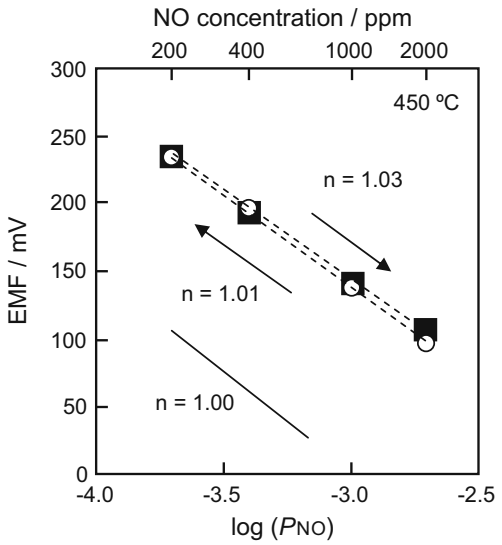

Fig. 20 The relationship between the sensor output (EMF) and the logarithm of the NO gas content at 450°C. (Reproduced with permission from [42]. Copyright 2004 The Electrochemical Society Inc.)

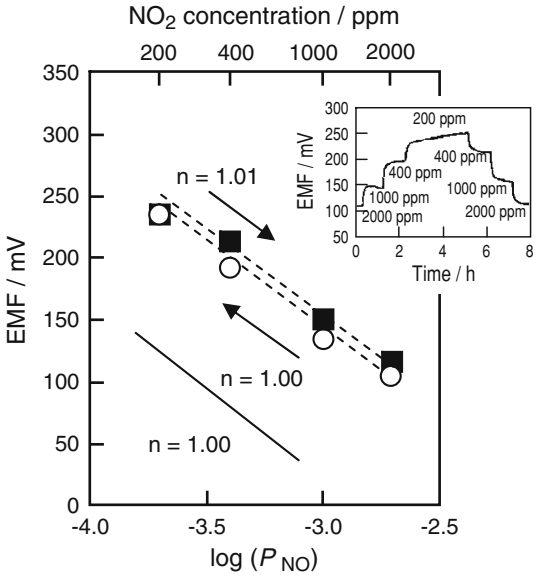

Fig. 21 The relationship between the sensor EMF output (EMF) and the logarithm of the NO_2 gas content at 450°C. Typical sensor response with NO_2 concentration variation (200–2,000 ppm) is also depicted as an inserted figure. (Reproduced with permission from [42]. Copyright 2004 The Electrochemical Society Inc.)

and the Nernst equation can be similarly described as follows.

$$E = E_0'' - (RT/nF)\ln(P_{NO_2}) \quad \left(E_0'' = \text{constant},\ n = 1.00\right) \tag{19}$$

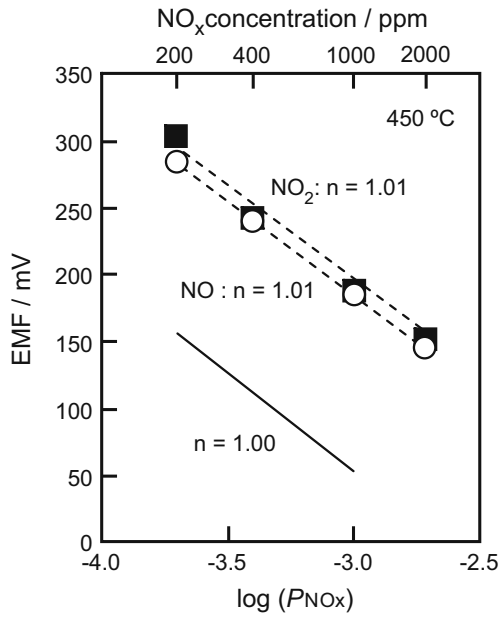

Fig. 22 The relationship between the sensor EMF output (EMF) and the logarithm of the NO (○) or NO_2 (■) gas content at 450°C. (Reproduced with permission from [42]. Copyright 2004 The Electrochemical Society Inc.)

The sensor EMF output for increasing (closed squares) and decreasing (open circles) NO_2 differed little similar as was also true for the n values of n=1.01 and 1.00, respectively. By comparing the EMF output sensing characteristics of Figs. 20 and 21, the present sensor is expected to operate by responding to the total in-situ NOx (NO plus NO_2) concentration.

The relationship between the sensor output and the logarithm P_{NO} (in decreasing) or NO_2 (in increasing) gas content at 450°C is presented in Fig. 22 [42]. This suggests that the sensor EMF output is consistent with total NOx, that is, NO plus NO_2 gas content can be detected by the present sensor cell.

Figure 23 depicts the sensor output during the variation of the NO and NO_2 gas content ratio with the total NO_X gas concentration maintained constant at 2,000 ppm [42]. By varying the NO and NO_2 gas ratio from 9:1 to 1:9, no meaningful EMF output deviation was observed. This demonstrates that the present sensor can detect the total NOx gas concentration, irrespective of the NO and NO_2 variation in total NOx gases.

3 Conclusions

An extraordinary high Al^{3+} ion conducting polycrystalline solid electrolyte $(Al_xZr_{1-x})_{4/(4-x)}Nb(PO_4)_3$ was successfully realized by stabilizing the NASICON type structure having a suitable three dimensional Al^{3+} ion pathway. The Al^{3+} ion conducting solid includes higher valent Nb^{5+} in addition to Zr^{4+} and P^{5+}. The level of Al^{3+} ion conductivity compares favorably with the ion conductivities typical of commercially available stabilized zirconia oxide anion conducting

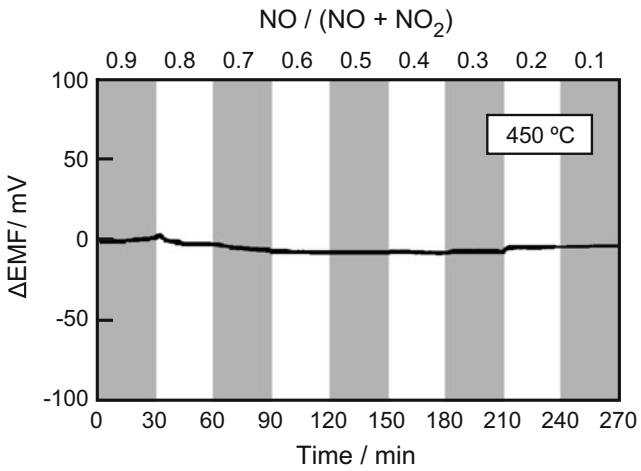

Fig. 23 The sensor output (EMF) deviation with the change of the NO and NO_2 gas ratio at 450°C. Total NO and NO_2 gas content is constant at 2,000 ppm. (Reproduced with permission from [42]. Copyright 2004 The Electrochemical Society Inc.)

solids such as yttria (YSZ) and calcia (CSZ) stabilized zirconia.

For the purpose of improving mechanical strength and density, boron oxide was added to the Al^{3+} ion conducting $(Al_{0.2}Zr_{0.8})_{20/19}Nb(PO_4)_3$ solid as a sintering additive. The B_2O_3 dissolved into the grain boundaries of the polycrystalline solid, and then vaporized during the sintering procedure leading to reduced porosity and improved contact between individual grains (The highest mechanical strength and the highest trivalent ion conductivity were successfully achieved for the $(Al_{0.2}Zr_{0.8})_{20/19}Nb(PO_4)_3$ solid electrolyte with 6 wt% B_2O_3 addition.). This composition was utilized in the development of a practical chemical gas sensor.

A CO_2 gas sensor was fabricated by combining the Al^{3+} ion conducting $(Al_{0.2}Zr_{0.8})_{20/19}Nb(PO_4)_3$ solid and O^{2-} ion conducting yttria stabilized zirconia (YSZ) with the auxiliary CO_2 gas sensing auxiliary electrode. Rapid and reproducible CO_2 detection and response were successfully realized at 500°C, by obeying the predicted Nernstian relationship. This sensor also shows high selectivity for CO_2 gas without interference by water vapor, NO, and O_2.

A practically applicable compact CO_2 sensor device was fabricated by using Al^{3+} and O^{2-} ion conducting solid electrolytes with auxiliary CO_2 gas sensing electrode with dimensions as small as 2 mm×3 mm×1 mm and electric power consumption down to approximately 0.6 W.

The trivalent Al^{3+} ion conducting solid was also examined as a means of monitoring total nitrogen oxides (NOx) with a similar combination of divalent O^{2-} ion conducting YSZ solid and the auxiliary NOx sensing electrode. The sensor shows similar EMF output both for NO and NO_2 gas detection, obeying the Nernst theoretical relationship, indicating a high total NOx gas sensing performance.

Since the Al^{3+} ion conducting solid electrolyte is a unique material, it is expected to be applied not only in the chemical gas sensor area but also for various other devices, such as rechargeable batteries, displays, etc.

References

1. T. Kudo, K. Fueki, *Solid State Ionics* (Kodansha, Tokyo, 1990)
2. P.G. Bruce, *Solid State Electrochemistry* (Cambridge, Cambridge University Press, 1995)
3. P.J. Gellimgs, H.J.M. Bouwmeester, *The CRC Handbook of Solid State Electrochemistry* (CRC, New York, 1997)
4. N. Imanaka, Y. Kobayashi, G. Adachi, Chem. Lett. **24**, 433 (1995). doi:10.1246/cl.1995.433
5. Y. Kobayashi, T. Egawa, S. Tamura, N. Imanaka, G. Adachi, Chem. Mater. **9**, 1649 (1997). doi:10.1021/cm970004b
6. J. Köhler, N. Imanaka, G. Adachi, Z. Anorg. Allg. Chem. **625**, 1890 (1999). doi:10.1002/(SICI)1521-3749(199911)625:11<1890::AID- ZAAC1890>3.0.CO;2-E
7. N. Imanaka, Y. Kobayashi, K. Fujiwara, T. Asano, Y. Okazaki, G. Adachi, Chem. Mater. **10**, 2006 (1998). doi:10.1021/cm980157e
8. S. Tamura, T. Egawa, Y. Okazaki, Y. Kobayashi, N. Imanaka, G. Adachi, Chem. Mater. **10**, 1958 (1998). doi:10.1021/cm980115q
9. N. Imanaka, M. Hiraiwa, S. Tamura, G. Adachi, H. Dabkowska, A. Dabkowski, J.E. Greedan, Chem. Mater. **10**, 2542 (1998). doi:10.1021/cm980306t
10. J. Köhler, N. Imanaka, G. Adachi, Chem. Mater. **10**, 3790 (1998). doi:10.1021/cm980473t
11. N. Imanaka, T. Ueda, Y. Okazaki, S. Tamura, G. Adachi, Chem. Mater. **12**, 1910 (2000). doi:10.1021/cm990591w
12. D.W. Strickler, W.G. Carlson, J. Am. Ceram. Soc **47**, 122 (1964). doi:10.1111/j.1151-2916.1964.tb14368.x
13. J.B. Goodenough, H.Y.P. Hong, J.A. Kafalas, Mater. Res. Bull. **11**, 203 (1976). doi:10.1016/0025-5408(76)90077-5
14. S. Tamura, N. Imanaka, G. Adachi, Solid State Ion. **136–137**, 427 (2000). doi:10.1016/S0167-2738(00)00552-X
15. S. Tamura, N. Imanaka, G. Adachi, J. Alloy. Comp. **323–324**, 540 (2001). doi:10.1016/S0925-8388(01)01139-2
16. R.D. Shannon, Acta Crystallogr. A **32**, 751 (1976). doi:10.1107/S0567739476001551
17. N. Imanaka, Y. Hasegawa, M. Yamaguchi, M. Itaya, S. Tamura, G. Adachi, Chem. Mater. **14**, 4481 (2002). doi:10.1021/cm020667f
18. S. Tamura, N. Imanaka, G. Adachi, Adv. Mater. **11**, 64 (1999). doi:10.1002/(SICI)1521-4095(199901)11:1<64::AID-ADMA64>3.0.CO;2-C
19. Y. Hasegawa, S. Tamura, N. Imanaka, J. N. Mater. Electrochem. Sys **8**, 203 (2005)
20. S. Yao, S. Hosohara, Y. Shimizu, N. Miura, H. Futata, N. Yamazoe, Chem. Lett. **20**, 2069 (1991). doi:10.1246/cl.1991.2069
21. S. Yao, Y. Shimizu, N. Miura, N. Yamazoe, Jpn. J. Appl. Phys. **31**, L197 (1992). doi:10.1143/JJAP.31.L197
22. S. Yao, Y. Shimizu, N. Miura, N. Yamazoe, Appl. Phys. A **57**, 25 (1993). doi:10.1007/BF00331212
23. N. Imanaka, T. Murata, G. Adachi, Denki Kagaku **61**, 909 (1993)
24. N. Imanaka, Y. Hirota, G. Adachi, Sens. Actuators B Chem **24/25**, 380 (1995). doi:10.1016/0925-4005(95)85085-6
25. S. Ikeda, S. Kato, K. Nomura, K. Ito, H. Einaga, S. Saito, Y. Fujita, Solid State Ion. **70/71**, 569 (1994). doi:10.1016/0167-2738(94)90374-3
26. S. Ikeda, T. Kondo, S. Kato, K. Ito, K. Nomura, Y. Fujita, Solid State Ion. **79**, 354 (1995). doi:10.1016/0167-2738(95)00087-M
27. N. Imanaka, M. Kamikawa, G. Adachi, Anal. Chem. **74**, 4800 (2002). doi:10.1021/ac011284o
28. N. Imanaka, A. Ogura, G. Adachi, Electrochemistry **71**, 14 (2003)
29. N. Imanaka, A. Oda, S. Tamura, G. Adachi, T. Maekawa, T. Tsumeishi, H. Ishikawa, Electrochem. Solid-State Lett. **7**, H12 (2004). doi:10.1149/1.1640492
30. S. Tamura, I. Hasegawa, N. Imanaka, T. Maekawa, T. Tsumiishi, K. Suzuki, H. Ishikawa, A. Ikeshima, Y. Kawabata, N. Sakita, G. Adachi, Sens. Actuators B Chem. **108**, 359 (2005). doi:10.1016/j.snb.2004.11.080
31. T. Maekawa, Y. Kawabata, Y. Nakazato, H. Ishikawa, S. Tamura, N. Imanaka, G. Adachi, Electrochemistry **74**, 118 (2006)
32. Y. Shimizu, Y. Okamoto, S. Yao, N. Miura, N. Yamazoe, Denki Kagaku **59**, 465 (1991)
33. N. Rao, C.M. Van den Bleek, J. Schoonman, Solid State Ion. **52**, 339 (1992). doi:10.1016/0167-2738(92)90181-N
34. S. Yao, Y. Shimizu, N. Miura, N. Yamazoe, Chem. Lett. **21**, 587 (1992). doi:10.1246/cl.1992.587
35. S. Yao, Y. Shimizu, N. Miura, N. Yamazoe, Chem. Lett. **22**, 193 (1993). doi:10.1246/cl.1993.193
36. N. Miura, S. Yao, Y. Shimizu, N. Yamazoe, Sens. Actuators B Chem. **13–14**, 387 (1993). doi:10.1016/0925-4005(93)85408-3

37. N. Miura, M. Iio, G. Lu, N. Yamazoe, Sens. Actuators B Chem. **35**, 124 (1996). doi:10.1016/S0925-4005(97)80041-X
38. Y. Shimizu, K. Maeda, Chem. Lett. **25**, 117 (1996). doi:10.1246/cl.1996.117
39. N. Miura, G. Lu, N. Yamazoe, H. Kurosawa, M. Hasei, J. Electrochem. Soc. **143**, L33 (1996). doi:10.1149/1.1836448
40. M.L. Grilli, E.D. Bartolomeo, E. Traversa, J. Electrochem. Soc. **148**, H98 (2001). doi:10.1149/1.1386921
41. N. Miura, M. Nakatou, S. Zhuiykov, Electrochem. Commun. **4**, 284 (2002). doi:10.1016/S1388-2481(02)00266-7
42. N. Imanaka, A. Oda, S. Tamura, G. Adachi, J. Electrochem. Soc. **151**, H113 (2004). doi:10.1149/1.1688343
43. G. Adachi, N. Imanaka, Chem. Rev. **98**, 1479 (1998). doi:10.1021/cr940055h
44. R.M. Williams, B.J. Nakamura, M.L. Underwood, M.A. Ryan, D. O'connor, S. Kikkert, Solid State Ion. **53–56**, 806 (992). doi:10.1016/0167-2738(92)90258-Q
45. Y.W. Kim, A. Oda, N. Imanaka, Electrochem. Commun. **5**, 94 (2003). doi:10.1016/S1388-2481(02)00537-4
46. Y.W. Kim, T. Masui, A. Oda, S. Tamura, N. Imanaka, Phys. Stat. Sol. A **198**, 369 (2003)